Nano Research

Open Access

Research Article

A bionic compound eye for quantitative detection of exosomes

Yuanyuan Liu, Jinxiu Wei, Tingyu Wang, Xuemeng Li, Kuo Yang, Zhuyuan Wang, Lei Wu ✉, Shenfei Zong ✉, and Yiping Cui

Advanced Photonics Center, School of Electronic Science & Engineering, Southeast University, Nanjing 210096, China

Cite this article: *Nano Research*, 2025, *18*, 94907203. https://doi.org/10.26599/NR.2025.94907203

ABSTRACT: Exosomes are important cancer biomarkers, however, the accuracy of exosome detection is greatly reduced due to heterogeneity of each exosome. Detecting exosomes with a larger field-of-view (FOV) might be a good solution. Compound eyes offer unique advantages such as a large field of view, low aberration, and high temporal resolution. Bionic compound eyes aim to replicate such features and have broad applications in fields like machine vision and medical imaging. In this paper, we propose the fabrication and application of a bionic compound eye for quantitative detection of exosomes, which allows fluorescence imaging of exosomes with an enlarged FOV, achieving a detection limit as low as 9.1 × 10^2 particles/mL. The bionic compound eye is formed by simply replicating a fly eye with polydimethylsiloxane (PDMS). To detect exosomes, a microfluidic array chip compatible with the compound eye is designed. Exosomes are captured on the chip using CD63 aptamers as the capturing probes. Another kind of fluorescent aptamers are utilized to recognize the captured exosomes. Large FOV dual-color fluorescence (LFDF) imaging of these exosomes is realized by inserting the compound eye between the objective and microfluidic chip. The advantages of LFDF imaging include, first, dual-color fluorescence imaging can guarantee that we are indeed imaging exosomes; second, large FOV can reduce the impact of heterogeneity of exosomes. Thus, the reliability of assay results would be greatly improved. As a proof-of-concept, breast cancer exosomes were used as the example. The experimental results showed that, compared to imaging without the compound eye, the standard deviation of LFDF imaging results decreased by approximately 38%. Thus, the detection errors could be greatly reduced. The feasibility of using LFDF imaging for subtype classification of breast cancer exosomes was also preliminarily validated. This technology offers a new, low-cost, and highly accurate solution for exosome based cancer diagnosis.

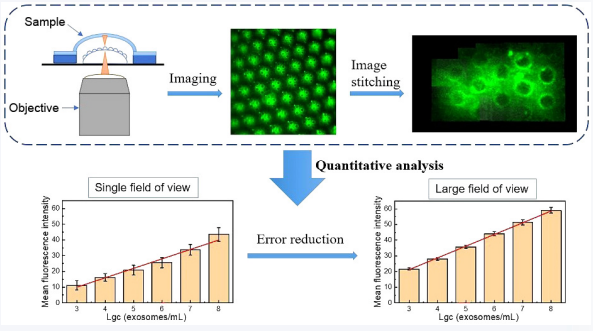

KEYWORDS: bionic compound eye, exosomes, large field-of-view, dual-color fluorescence imaging

1 Introduction

Exosomes are extracellular vesicles secreted by eukaryotic cells, playing a key role in intercellular communication. Recent studies have revealed a substantial rise in the levels of exosomes in individuals with cancer, highlighting their critical involvement in tumor development and metastasis [1, 2]. Membrane proteins and miRNA on exosomes can serve as biomarkers for cancer diagnosis [2–4]. However, the high heterogeneity of exosomes poses a significant challenge for precise cancer diagnosis. Exosomes consist of different subtypes, containing various proteins, nucleic acids, lipids, and other components. The relative abundance of these compounds is influenced by the cell type of origin and the physiological state of the individual cells [5, 6]. The blood used for liquid biopsy contains a large variety of exosome subtypes. Consequently, when the quantity of exosome samples is insufficient, it can lead to considerable diagnostic errors, hindering accurate cancer diagnosis. In recent years, various methods for exosome detection have been developed, such as colorimetry, electrochemistry, surface-enhanced Raman scattering (SERS), fluorescence, etc. [7–11]. These methods have been combined with microfluidic technology to improve detection efficiency [12, 13]. While these methods hold significant promise, their application in practical clinical diagnostics is currently limited by the low throughput and poor sensitivity. Continued efforts are still needed to develop efficient, reliable, and cost-effective exosome detection technologies.

Compound eyes are visual organs found in insects, arthropods,

Received: August 19, 2024; Revised: December 17, 2024
Accepted: December 18, 2024

✉Address correspondence to Lei Wu, lwu@seu.edu.cn; Shenfei Zong, sfzong@seu.edu.cn

and crustaceans in the natural world [14]. Within the visual field of compound eyes, objects in different directions can be captured by the corresponding angles of ommatidia, and there are overlapping regions between adjacent ommatidia's visual fields, which can avoid blind spots. Due to its unique structure, insect compound eyes have advantages such as high temporal resolution and a large field of view (FOV) [15, 16]. Bionic compound eyes, distinguished by their small size, high integration, and large field of view, have attracted much attention in recent years, addressing many issues existing in single-aperture optical systems. Therefore, this study aims to leverage the wide field of view of bionic compound eyes to increase the number of exosome samples analyzed in a single experiment, thereby improving the accuracy of cancer diagnosis. Bionic compound eyes are generally divided into two categories based on their external geometry: planar bionic compound eyes and curved bionic compound eyes [17]. Early research primarily focused on planar bionic compound eyes, which are simple in structure, easy to manufacture, and compatible with CCD or CMOS planar photodetectors [18, 19]. However, planar bionic compound eyes have a small field of view and low light utilization efficiency [20]. Curved bionic compound eyes closely mimic the structure and optical characteristics of natural biological compound eyes and have a higher light utilization efficiency and larger field of view compared to planar bionic compound eyes. Therefore, researchers mainly focused on studying curved bionic compound eye systems. Currently, various techniques such as inkjet printing, femtosecond laser two-photon polymerization, nanoimprinting, femtosecond laser wet etching, etc., have been used to manufacture compound eye structures [21–23]. Different types of microlens arrays have been developed, showing tremendous potential in imaging fields like photonics and biomedical sciences [24–26]. However, these fabrication techniques rely on complex, high-precision instruments and still require the development of simple and cost-effective methods to facilitate large-scale production. Additionally, the manufactured curved microlens arrays have defects, and their performance cannot fully match that of natural compound eyes.

To address the challenge of visualizing exosome heterogeneity, this paper proposes a large FOV dual-color fluorescence (LFDF) imaging method based on bionic compound eyes. By using polydimethylsiloxane (PDMS) to directly mold fly eyes, we obtained bionic compound eyes that closely resemble the structure and optical performance of natural compound eyes. We then designed a microfluidic chip with a micropillar array structure to capture breast cancer cell exosomes. Two fluorescently labeled aptamers were used to label exosome membrane proteins with dual color, eliminating false-positive results. We presented the more accurate quantification of exosomes using the bionic compound eye and explored the potential of this method in detecting clinical blood samples and classifying breast cancer subtypes. The LFDF imaging proposed in this paper increases the observable exosome sample quantity, reduces the standard deviation of experimental data, and effectively enhances the accuracy of quantitative exosome detection.

2 Results and discussion

2.1 Fabrication and performance characterization of bionic compound eye

Figure 1(a) illustrates the fabrication process of bionic compound eyes. Compound eyes dissected from fly specimens are placed on PDMS and heated together for curing. Subsequently, the compound eyes are completely separated from the PDMS to obtain a concave mold of the compound eyes. After hydrophobic treatment of the concave eye mold, a replica of the basic structure of bionic compound eyes is obtained through PDMS casting. Due to the thermal expansion coefficient of PDMS, there is approximately a 1% reduction in the size of the compound eye during the cooling process. This can cause changes in the focal length of the microlenses and introduce new aberrations. However, no significant interference caused by the reduction in size was observed in the experiments. To minimize deformation, we can opt for a lower curing temperature and a longer curing time. PDMS exhibits excellent flexibility and chemical stability, making it a convenient and cost-effective material for replication. Its high resolution allows precise replication of the intricate structures of compound eyes, and its high light transmittance ensures good optical performance of bionic compound eyes.

The fundamental structure of insect compound eyes consists of orderly arranged ommatidia distributed on a curved surface, where each ommatidium acts as a small lens affecting the imaging performance of the entire optical system. Figure 1(b) shows the scanning electron microscopy (SEM) image of the surface morphology of the bionic compound eye. The microlenses are arranged in a uniform hexagonal pattern, with a smooth surface, and the pore diameter ranges from 60 to 70 μm. It can be observed that PDMS can effectively replicate the structure of natural compound eyes, yielding bionic compound eyes with densely packed arrays of micro-lenses. Figure 1(c) shows the focusing situation of bionic compound eyes, with distinct focal points observable. In the experiment, bionic compound eyes are observed under a 10× microscopy objective to clearly reveal their specific structure. Additionally, it has been noted that image edges exhibit a tendency toward blurriness, which can be attributed to the arrangement of micro-lenses on a curved surface. This arrangement results in the focal points of ommatidia converging on a curved plane that diverges from the flat focal plane typically associated with microscopy objectives. Consequently, variations in the highest brightness of the focal centers of individual ommatidia are observed (Fig. 1(d)).

To characterize the optical performance of the fabricated PDMS bionic compound eyes, a mask plate engraved with the digits "4", the letter "F", and other patterns is produced using a three-dimensional (3D) printer. The compound eyes' response to the formed images is observed. Figure 1(e) illustrates the schematic diagram of the experimental setup. The mask plate with asymmetric patterns is placed between a white light source and the PDMS compound eyes. Beneath the compound eyes is a 10× microscopy objective. Light passing through the mask plate is focused and imaged by the compound eyes, and then captured and magnified by the objective lens. By adjusting the distances between the mask plate and the compound eyes, as well as between the compound eyes and the objective lens, clearer images can be observed. Figure 1(f) displays the images formed by different patterns in the central convex area of the bionic compound eyes. An evident array structure can be observed through the compound eyes. Due to the limited precision of the 3D-printed mask plate, some patterns only have outlines, yet these details can still be observed through the compound eyes. The results indicate that the target images are clear, and focus gradually disperses outward from the center of the compound eyes. The replicated micro-lens array structure is uniform, exhibiting excellent optical imaging performance.

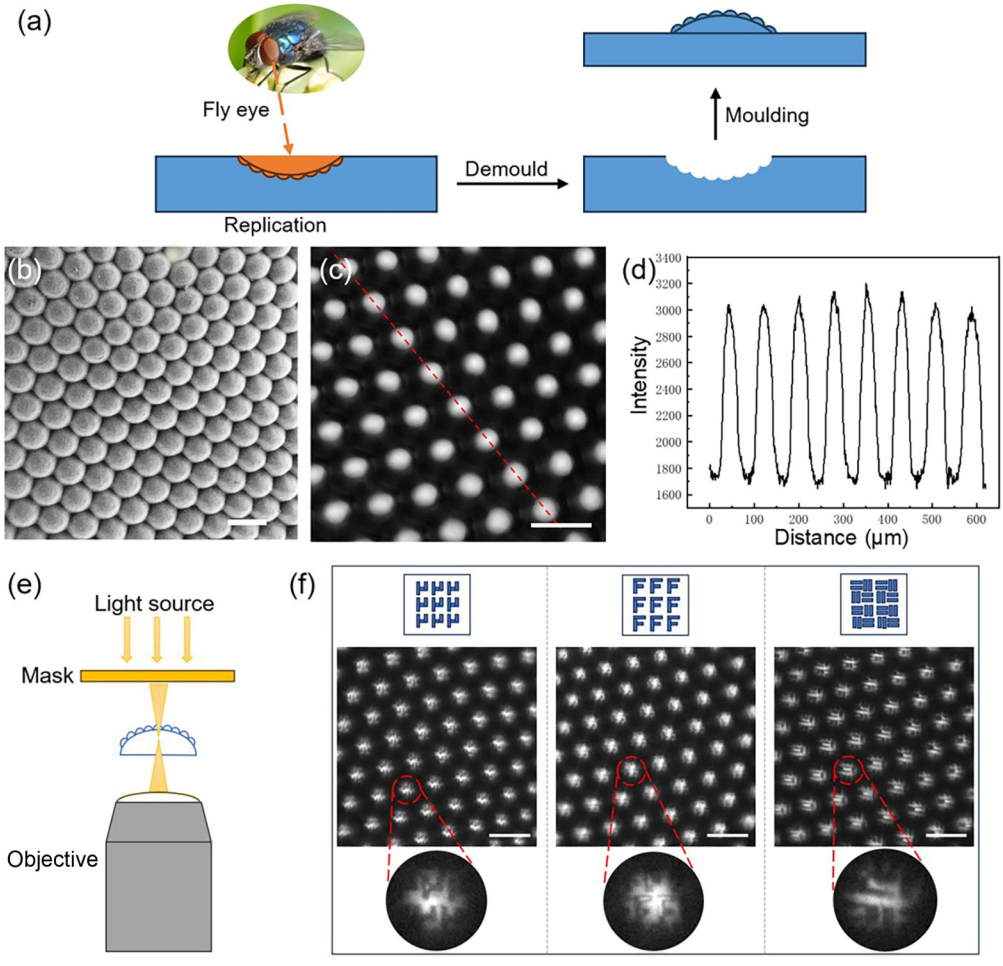

Figure 1 Fabrication process and optical performance of bionic compound eyes. (a) Schematic diagram of the preparation process of bionic compound eyes using PDMS through two-step replica molding of insect compound eyes. (b) SEM image of the bionic compound eye. (c) Focused image of the compound eyes under bright field illumination. (d) Intensity distribution along the red dashed line in (b). (e) Schematic diagram of the experimental setup for testing the imaging performance of the compound eyes. (f) Images obtained by the compound eyes of the digits "4", the letter "F", and an asymmetric pattern array, as well as an enlarged image of one ommatidium. Scale bar: 100 μm.

In order to validate the compatibility of the bionic compound eyes with the laser path before subsequent experiments, it is necessary to confirm whether the compound eyes match the laser path. In the experiment, quantum dots excited by a 405 nm laser with fluorescence emission around 605 nm are used. The quantum dot solution is injected into microfluidic channels, as depicted in Fig. 2(a). Figures 2(b) and 2(c) show the specific structure of a region in the microfluidic channels observed under a microscopy. The structure is relatively intact with strong fluorescence, although some areas of the solution have not reached, which does not affect its function. The microfluidic chip is fixed above the compound eyes and placed together on the microscopy stage. By adjusting the distance between the compound eyes and the objective lens, distinguishable images can be observed in the ommatidia. Figures 2(d) and 2(e) respectively show different regions of the microfluidic channels observed through the compound eyes by moving the microfluidic chip. Due to the large size of the microfluidic channels, only a certain rectangular area of the channels can be observed, allowing the basic structure of the channels to be distinguished, which indicate the feasibility of using the compound eyes for imaging fluorescent patterns.

Compared with other bionic compound eye systems, the biggest advantage of our compound eye is simplicity since our compound eye is directly obtained by molding the eye of a fly. A possible defect is that, since the parameters of the fly eye are fixed, the compound eye we obtained would show a poor adjustability. For example, each ommatidium is distributed on a curved surface, resulting in the overall imaging of the compound eye occurring also on a curved surface. In contrast, other compound eye imaging systems can adjust parameters such as the curvature radius and aperture of the ommatidia to project the images from different ommatidia onto a single plane, making them more compatible with other imaging systems.

2.2 Quantitative detection of exosomes exploiting the wide-field of bionic compound eye

To investigate the practical application of bionic compound eyes, we chose exosomes as the detection targets. Exosomes carry various substances such as cell-specific proteins, lipids, and nucleic acids, making them typical tumor markers [27]. Due to the extremely small size of exosomes, imaging of single markers alone cannot confirm their presence. Therefore, we employed a dual-marker detection approach to ensure high accuracy. Moreover, transferring exosome detection into microfluidic chips can significantly reduce the amount of reagents and samples used in experiments, thereby

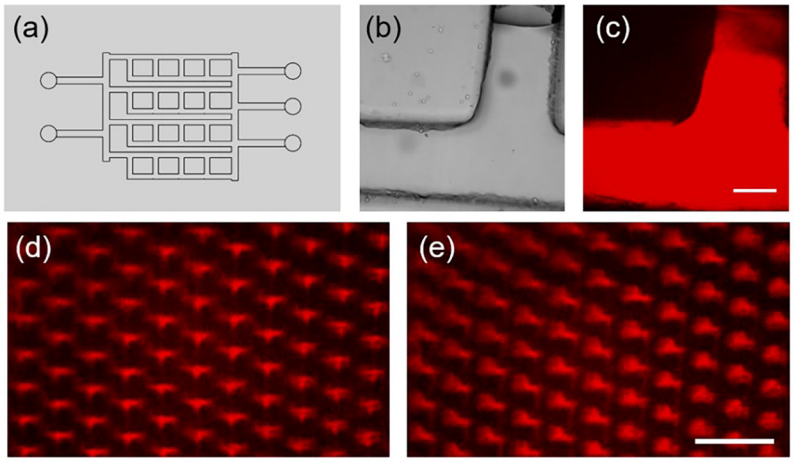

Figure 2 Bionic compound eyes imaging test of fluorescent patterns. (a) Schematic diagram of microfluidic channels. (b) Structure of channels observed under bright field microscopy. (c) Image observed in quantum dot channels. (d) and (e) Images obtained by compound eyes in different regions of microfluidic channels. Scale bar: 100 μm.

reducing costs and shortening reaction times. The specific experimental scheme is illustrated in Fig. 3(a). Firstly, a layer of polyethyleneimine (PEI) is modified on the channel surface through electrostatic adsorption. Then, glutaraldehyde (GA) and CD63 aptamer (modified with amino) are modified through the reaction between amino and aldehyde groups, used to capture exosomes in the solution. After exosomes are captured on the channel surface, aptamers labeled with Cy5 fluorescent dye and Alexa Fluor 568 fluorescent dye are introduced immediately. These aptamers are specific to epithelial cell adhesion molecule (EpCAM) and human epidermal growth factor receptor 2 (HER2) proteins on the exosome membrane, respectively, enabling dual-color fluorescence labeling. We characterized the exosomes derived from SK-BR-3. Figure S1 in the Electronic Supplementary Material (ESM) shows the image of SK-BR-3 exosomes observed by transmission electron microscopy (TEM), revealing a distinct concave structure. Additionally, we performed western blot (WB) analysis on the exosomes, and the results indicated a high expression of EpCAM and HER2 in SK-BR-3 exosomes (Fig. S2 in the ESM).

Due to the high heterogeneity of exosomes and their uneven distribution within microfluidic chips, achieving accurate quantification of exosome membrane proteins requires multiple observations of different regions of the sample to obtain more sample information and reduce diagnostic errors. Compound eyes can perceive information from multiple directions simultaneously, enabling large-field imaging. To facilitate subsequent wide-field image stitching and sample analysis, we designed boat-shaped microfluidic channels with micro-pillar arrays. The structure of the microchannel is shown in Figs. 3(b)−3(d). Each PDMS micro-pillar has a diameter of 300 μm and a height of 200 μm, and exosomes are captured and reacted outside the micro-pillar array region. SK-BR-3 exosome stock solutions of different concentrations were separately diluted and introduced into the PDMS chip for experiments, while other experimental conditions remained unchanged. Imaging results directly obtained through a microscopy objective (i.e., without using bionic compound eyes) are shown in Figs. 3(e) and 3(f). Complete circular arrays can be observed under the microscopy, indicating a tight fit between the two PDMS layers and a well-structured array. Distinct fluorescent spots can be observed outside the cylindrical region in both EpCAM and HER2 channels, indicating high expression levels of EpCAM and HER2 on SK-BR-3 cell-derived exosomes, with the positions of the spots in both channels largely overlapping. The Pearson correlation coefficient (PCC) obtained through ImageJ software analysis of the images from both channels is 0.71. These results indicate successful labeling of the exosome surface with fluorescent aptamer probes. Additionally, there is a brighter ring of fluorescence around the pillar, which is due to the limited spatial resolution of 3D printing, reaching up to 25 μm. The printed cylinders are not smooth around their perimeters, containing many irregularities. Exosomes are easily trapped in these irregularities, and the accumulation of numerous exosomes results in stronger fluorescence. Therefore, when performing quantitative analysis, it is necessary to avoid the brighter ring around the pillar. From Figs. 3(e) and 3(f), it can be observed that as the concentration of exosomes decreases, the number of fluorescent spots in the chip reaction area decreases, and the overall fluorescence intensity of the image decreases. Therefore, quantitative analysis of exosome concentration can be achieved by selecting specific regions and analyzing their average fluorescence intensity.

In ImageJ software, the fluorescence intensity information contained in the image is converted into gray values between 0 and 255. In a single image, we selected four regions using circular region of interest (ROI) (as shown in Figs. 3(e) and 3(f)), and calculated the average gray values and standard deviations of these four regions. These four regions are the largest circular regions that can be selected within the reaction area, aiming to cover the maximum possible area of the reaction region. The results are presented in the bar graphs in Figs. 3(g) and 3(h), with error bars representing standard errors. The initial concentration of the exosome samples was determined using nanoparticle tracking analysis (NTA). As the exosome concentration decreases, fewer exosomes will be captured on the surface of the microfluidic channel, leading to a lower density of fluorescence spots. This results in a decrease in the observed average fluorescence intensity within a given region. We used ImageJ software to calculate the average grayscale value of the images, which reflects the average fluorescence intensity. It can be observed that as the concentration of exosome samples increases, the average fluorescence intensity of both the EpCAM and the HER2 channels also increases, with the overall fluorescence intensity of the EpCAM channel being greater than that of the

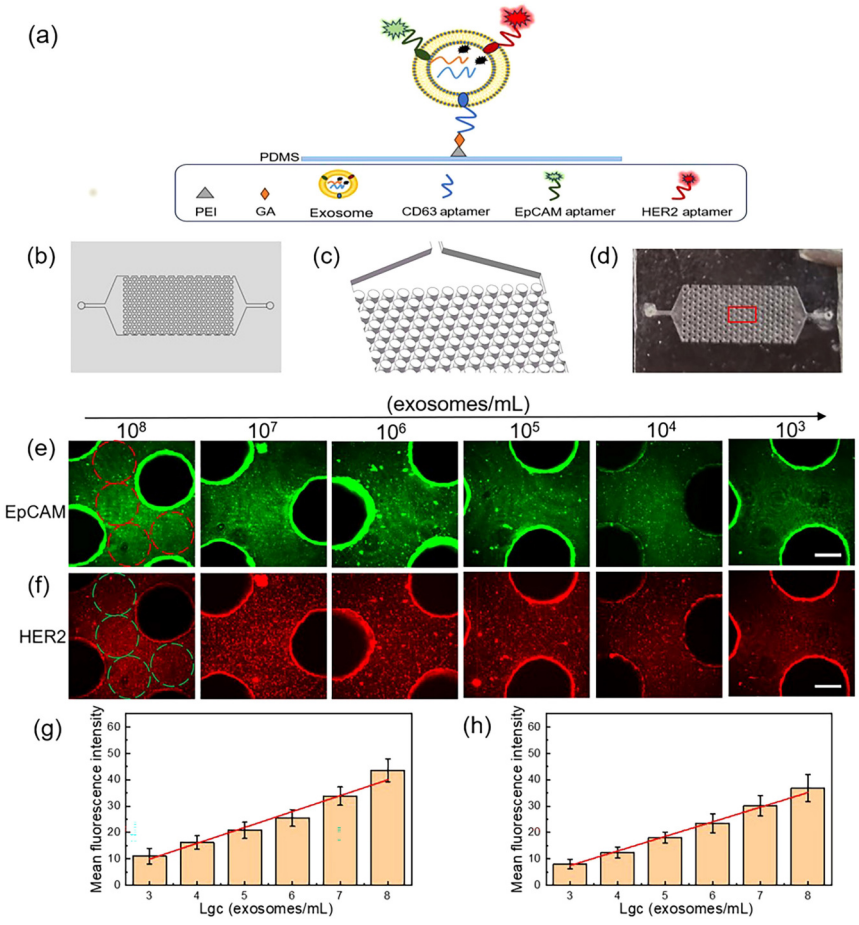

Figure 3 Direct imaging of different concentrations of SK-BR-3 exosomes using a microscopy objective. (a) Schematic diagram illustrating the principle of exosome membrane protein detection. Schematic diagram of the microfluidic chip channel (b) and the internal structure of the chip (c). (d) Photograph of the microfluidic chip. The area enclosed by the red box is the imaging region of the compound eye on the PDMS chip in Fig. 4. (e) Imaging results of EpCAM membrane protein for SK-BR-3 exosomes at different concentrations. (f) Imaging results of HER2 membrane protein for SK-BR-3 exosomes at different concentrations. Scale bar: 100 μm. (g) Average fluorescence intensity and standard deviation of the EpCAM channel, along with curve fitting results, analyzed from (e). (h) Average fluorescence intensity and standard deviation of the HER2 channel, along with curve fitting results, analyzed from (f).

HER2 channel. This is because as the concentration of exosomes in the solution increases, the probability of exosomes being captured on the channel surface increases, resulting in more observed fluorescence spots. However, it is also noted that the standard deviations obtained from the histograms are relatively large, indicating that the fluorescence intensity alone is not sufficient for accurate quantification of exosome concentration in practical detection. This is because exosomes are not uniformly distributed on the channel surface, and the density of fluorescence spots varies in different regions, leading to deviations in the average fluorescence intensity.

To observe a larger area of the microfluidic chip, we placed the chip above the bionic compound eyes for imaging. Firstly, the compound eyes are formed by closely arranged microlenses on a nearly spherical surface. Therefore, light passing through the microlenses converges on a curved surface, requiring the compound eyes to be rotated to observe different regions on the focal plane. Secondly, during the rotation process, the distance between the objective lens and the compound eyes remains approximately constant. To ensure that the image formed by the sample passing through the compound eyes always remains at the focal point of the objective lens, the sample should also approximate a curved surface to maintain a nearly constant distance between the sample and the compound eyes. Through measurement and calculation, the overall curvature radius of the compound eyes is determined to be 8 mm, and the distance between the sample and the compound eyes is designed to be 2 mm. Therefore, the flexible PDMS chip is bent and fixed on a curved platform with a curvature radius of 10 mm, which is then placed above the compound eyes. Figure 4(a) illustrates the principle of expanding the FOV using a bionic compound eye. By rotating the compound eye along with the arched chip, different regions of the chip can be observed through the objective lens and the compound eye. Additionally, to ensure that the images formed by the ommatidia after each rotation overlap partially for subsequent image registration, the rotation angle is set to be 3° each time. As shown in Figs. 4(b) and 4(c), images of EpCAM and HER2 membrane proteins are obtained by synchronously rotating the compound eyes and the PDMS chip by 0°, 3°, 6°, and 9°. Clear circular arrays can be observed in each ommatidium, and the observed sample area changes as the angle increases.

Next, clear images of partial ommatidia from different angles were selected from the images, and our scale-invariant feature transform (SIFT)-based image stitching algorithm was employed to stitch these partial ommatidial images together into a large FOV image. The results of image stitching are shown in Figs. 4(d) and

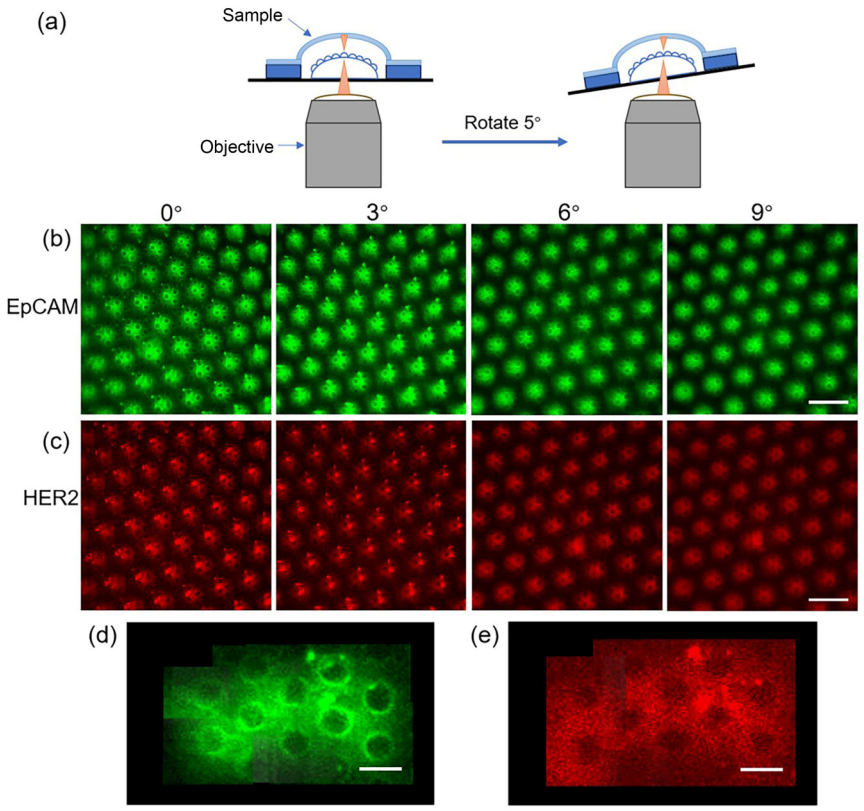

Figure 4 LFDF imaging of SK-BR-3 cell-derived exosomes based on bionic compound eyes. (a) Schematic diagram of expanding the observation area by rotating the compound eye and the sample. (b) Fluorescence images of EpCAM protein channel observed under the microscopy as the compound eyes and the sample synchronously rotate by 0°, 3°, 6°, and 9°, respectively. Scale bar: 100 μm. (c) Fluorescence images of HER2 protein channel observed under the microscopy as the compound eyes and the sample synchronously rotate by 0°, 3°, 6°, and 9°, respectively. (d) Stitched result of images at various angles for the EpCAM channel. (e) Stitched result of images at various angles for the HER2 channel. Scale bar: 20 μm.

4(e). During the stitching process of images at 0°, 3°, 6°, and 9°, the images formed by the ommatidia are stitched into the large image from right to left. The final stitched large FOV image covers an area approximately 8 times larger than the area observed in a single microscopy field of view shown in Figs. 3(e) and 3(f), demonstrating the significant advantage of the compound eyes in providing a large FOV.

Subsequently, exosome samples were diluted to different concentrations, captured and labeled using flexible PDMS chips, and placed above the compound eyes for imaging. Figures 5(a)−5(f) and 5(g)−5(l) respectively show the fluorescence imaging results of the compound eyes for the EpCAM and HER2 proteins on the surface of exosomes. From the images, it can be observed that as the concentration of exosomes decreases, the fluorescence probes binding to the exosomes decrease, resulting in reduced fluorescence collected by the ommatidia and weakening of the fluorescence intensity in the images formed by the compound eyes. By analyzing the fluorescence intensity detected by the compound eyes, more accurate quantification of exosome concentration can be achieved. Using image stitching algorithms, images formed by exosome samples at different concentrations were stitched and processed. Then, the large FOV fluorescence images were imported into ImageJ, multiple regions were selected, and the average grayscale values of each region were calculated to obtain fluorescence intensity histograms as shown in Figs. 5(m) and 5(n), with error bars representing the standard deviation. Due to the focusing effect of the compound eyes on the microfluidic array chip, the fluorescence intensity in the images formed by the compound eyes was enhanced compared to that using direct imaging by the microscopy. It can be clearly observed that as the concentration of exosomes increases, the fluorescence intensity of both channels also increases, indicating an increase in the concentrations of EpCAM and HER2 membrane proteins. Furthermore, compared to the standard deviation of fluorescence intensity detected by a single field of view under the microscopy in Figs. 3(g) and 3(h), the standard deviation calculated from the large FOV images decreased by 38%, significantly improving the accuracy of the quantification of exosome concentration. This reduction in standard deviation is attributed to the eightfold increase in the FOV of the final image, allowing for the analysis of eight times larger sample areas. This means that larger areas can be selected to calculate the average fluorescence intensity, thereby obtaining more information. Analyzing a larger sample size of data can better assess the degree of variation in the data, allowing the standard deviation to more accurately reflect the true fluctuation of the data, without being influenced by individual extreme values. This enables a more accurate calculation of the average value of the data, making the results a better reflection of the whole data set. The results indicate that our LFDF imaging can observe a larger sample area, thereby obtaining more fluorescence intensity information from the sample. This reduces the standard deviation of the data and enhances the reliability and accuracy of exosome quantification results. Compared with some typical exosome detection methods include, SERS-based detection with an accuracy of up to 93% [28], label-free fluorescence detection with an accuracy of up to 85% [29], and aptamer-functionalized magnetic Ti_3C_2-based detection with an

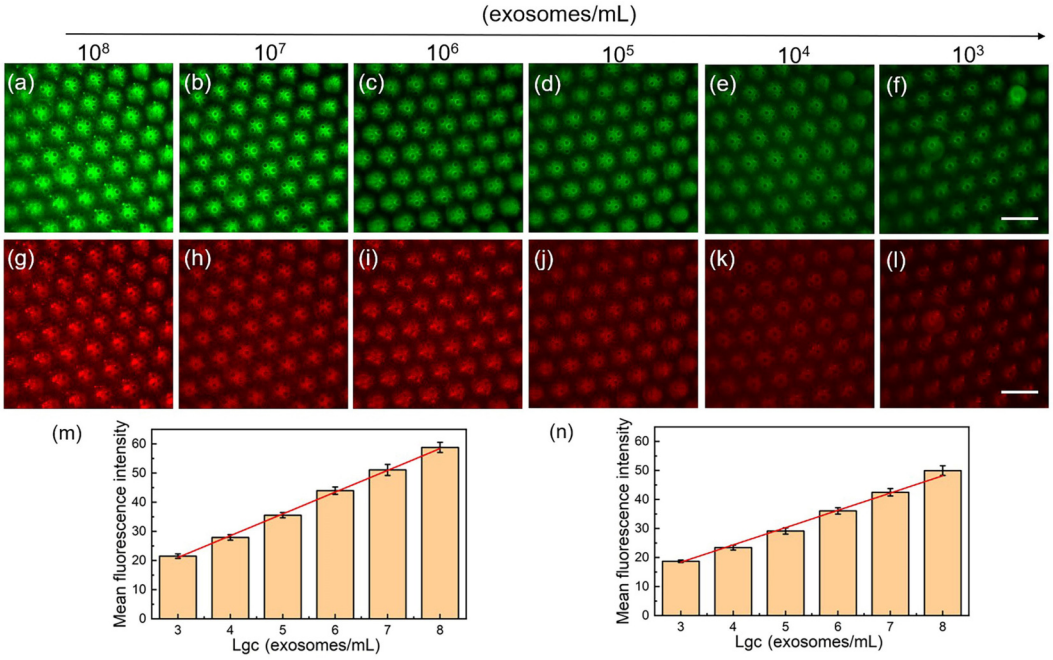

Figure 5 Quantitative detection of SK-BR-3 exosomes based on bionic compound eyes. (a)–(f) Fluorescence images of the EpCAM membrane protein formed by compound eyes for SK-BR-3 exosome samples at different concentrations. (g)–(l) Fluorescence images of the HER2 membrane protein formed by compound eyes for SK-BR-3 exosome samples at different concentrations. Scale bar: 100 μm. (m) and (n) Variation in fluorescence intensity with exosome concentration for the EpCAM channel and HER2 channel, along with the curve fitting results.

accuracy of 96%–99% [30], the method we propose demonstrates an accuracy of 98.7%–99.8%, which is superior to the previously reported methods to some extent. The detection limit of our method is 9.1 × 10^2 particles/mL, which is calculated when the detected fluorescence intensity is three times the background noise. This detection limit is superior to that of most other detection methods [31−33].

We used two batches of exosome samples and conducted experiments at 7 days, 1 month, and 6 months after extraction (Fig. S3 in the ESM). It can be observed that the fluorescence intensity slightly decreased after 1 month, but the change was not significant and had little impact on the experimental results. This demonstrates the good repeatability of our method.

2.3 Clinical sample detection of breast cancer

In clinical cancer diagnosis, real blood samples contain a variety of biomolecules, and extracellular vesicles exist in a more complex biological environment, making the detection process prone to false-positive signals. To investigate the ability of LFDF imaging to detect extracellular vesicles in blood, we spiked extracted SK-BR-3 extracellular vesicles into blood samples from healthy individuals to simulate a clinical blood environment. Meanwhile, another group of untreated healthy blood samples served as a control group. Both sets of blood samples were passed through a microfluidic chip for extracellular vesicle detection. Figures 6(a) and 6(b) show the EpCAM and HER2 channels of breast cancer blood samples observed directly above the objective lens of a microscopy. Both channels exhibit obvious fluorescent spots, indicating high expression of EpCAM and HER2 in the blood extracellular vesicles. Figures 6(c) and 6(d) depict the EpCAM and HER2 channels of healthy blood samples, where fewer fluorescent spots are visible in both channels, and the overall fluorescence intensity is significantly weaker compared to breast cancer blood samples.

Subsequently, the microfluidic chip was placed above a bionic compound eye for imaging of the two sample groups. Figures 6(e) and 6(f) depict the images formed by the compound eye for the EpCAM and HER2 channels of breast cancer blood samples, showing clear fluorescent array images with higher fluorescence intensity in the EpCAM channel compared to the HER2 channel. Figures 6(g) and 6(h) show the EpCAM and HER2 channels of healthy blood samples observed by the compound eye, with weaker fluorescence intensity in both channels. Additionally, the HER2 channel exhibits no distinct array structure, indicating lower expression levels of EpCAM and HER2 proteins. To further quantify the EpCAM and HER2 membrane proteins, ImageJ software was used to analyze the fluorescence intensity of the images. Figure 6(i) presents the average fluorescence intensity and the standard deviation obtained from the analysis of Figs. 6(a)−6(d), while Fig. 6(j) shows the average fluorescence intensity values obtained from imaging with the compound eye from multiple perspectives for large field-of-view analysis. It can be observed that the expression levels of HER2 and EpCAM membrane proteins in breast cancer blood samples are high, enabling differentiation from normal blood samples, indicating that LFDF imaging has potential feasibility for clinical breast cancer diagnosis. Furthermore, due to the compound eye's further focusing on the microfluidic chip, the average fluorescence intensity observed is enhanced, and the standard deviation of the average fluorescence intensity based on compound eye large field-of-view imaging is significantly reduced, increasing the accuracy of breast cancer diagnosis.

2.4 Analysis of breast cancer subtypes

Breast cancer is a highly heterogeneous disease, where different breast cancer patients may exhibit diverse pathological, molecular, and clinical characteristics. Subtyping breast cancer can aid doctors in better understanding the pathological and molecular features of patients, thereby enabling the selection of personalized treatment plans. Additionally, breast cancer subtype analysis can provide

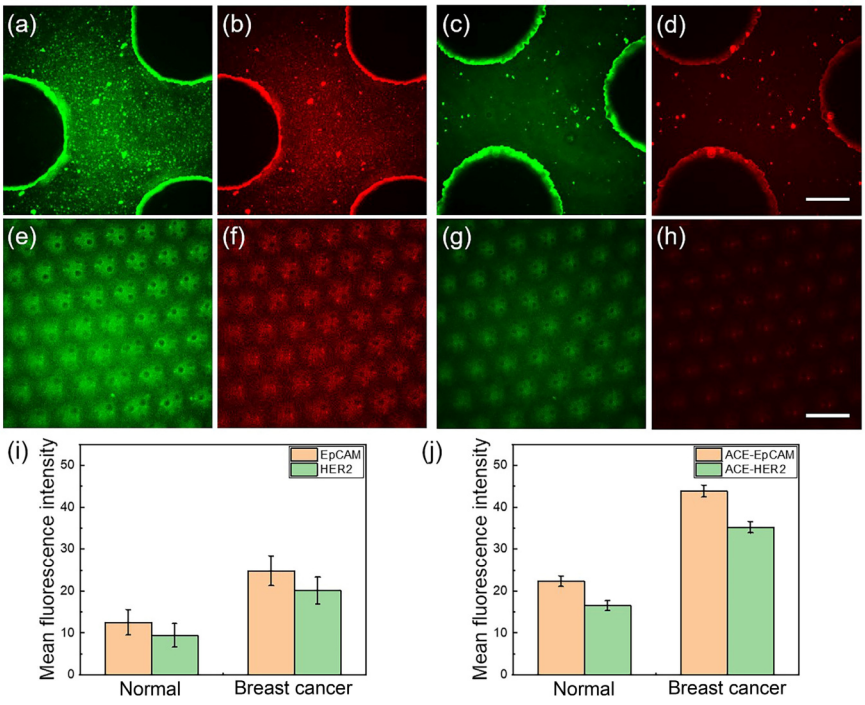

Figure 6 Results of extracellular vesicle detection in simulated breast cancer blood samples. EpCAM channel (a) and HER2 channel (b) of breast cancer blood samples observed directly under a 10× objective of a microscopy. EpCAM channel (c) and HER2 channel (d) of healthy blood samples observed directly under a 10× objective of a microscopy. EpCAM channel (e) and HER2 channel (f) of breast cancer blood samples observed using a bionic compound eye. EpCAM channel (g) and HER2 channel (h) of healthy blood samples observed using a bionic compound eye. Average fluorescence intensity obtained from imaging under a 10× objective of a microscopy (i) and from imaging with the compound eye (j). Scale bar: 100 μm.

insights into the molecular and pathogenic mechanisms of breast cancer, offering essential groundwork for clinical research and drug development. In our experiment, we selected three breast cancer subtype cells: SK-BR-3, MDA-MB-231, and MCF-7. We used EpCAM aptamers modified with Alexa Fluor 568 fluorescent dye, HER2 aptamers modified with Cy5 fluorescent dye, and epidermal growth factor receptor (EGFR) aptamers modified with FAM fluorescent dye, ensuring that the fluorescent signals from the three membrane protein channels do not overlap. The extracellular vesicle stock solution was diluted with phosphate buffered saline (PBS) solution to the same concentration and introduced into a PDMS microfluidic chip. Subsequently, the three membrane proteins were fluorescently labeled using the respective aptamers, and the imaging was performed using a bionic compound eye. Figure 7(a) displays the imaging results of SK-BR-3 extracellular vesicles, where distinct fluorescent spots are observed in all three membrane protein channels. However, the fluorescence intensity of the EGFR channel is weaker, resulting in the absence of a clear array structure in the compound eye observation. Figure 7(b) illustrates the imaging results of MDA-MB-231 extracellular vesicles, showing weak fluorescence and fewer fluorescence spots in the HER2 channel, indicating lower HER2 expression levels. Figure 7(c) presents the imaging results of MCF-7 extracellular vesicles, where compared to EpCAM and HER2, EGFR expression levels are lower. These fluorescence imaging results demonstrate that the three breast cancer subtype cells exhibit different levels of protein expression on the membrane.

To accurately assess the expression levels of the three membrane proteins in different cell lines and achieve the classification of breast cancer subtypes, we utilized ImageJ to analyze the fluorescence intensity. Figures 7(d) and 7(e) present the expression levels of different membrane proteins obtained through the analysis of average fluorescence intensity. Due to the reduction in standard error of the mean of the average fluorescence intensity obtained from the analysis of large field-of-view images formed by the compound eye, accurate differentiation of membrane proteins with similar expression levels can be achieved. For example, compared to Fig. 7(d), Fig. 7(e) clearly shows that the expression level of EpCAM in SK-BR-3 extracellular vesicles is higher than that of HER2. Furthermore, from the figures, it can be inferred that the expression levels of EpCAM and HER2 in SK-BR-3 extracellular vesicles are higher than those in the other two subtypes. MDA-MB-231 extracellular vesicles exhibit the lowest HER2 expression level and relatively higher EGFR expression level, and MCF-7 extracellular vesicles have lower expression levels of EpCAM and EGFR compared to the other two subtypes. Based on the expression levels of EGFR, EpCAM, and HER2 proteins on the surface of extracellular vesicles, the three vesicle populations can be clearly distinguished. Therefore, large-field fluorescence imaging of three membrane proteins on extracellular vesicles, based on the bionic compound eye, shows potential for more accurate subtyping of breast cancer.

3 Conclusions

In this work, we presented a simple and low-cost method for fabricating a bionic compound eye and utilized it for LFDF imaging of breast cancer exosomes, achieving more accurate exosome quantification with a detection limit as low as 9.1×10^2 particles/mL. A bionic compound eye with good optical performance was easily obtained by double molding with PDMS. To address the challenge of exosome heterogeneity, we applied the fabricated bionic compound eye to exosome detection. Two highly specific fluorescent aptamer probes were selected for dual-color

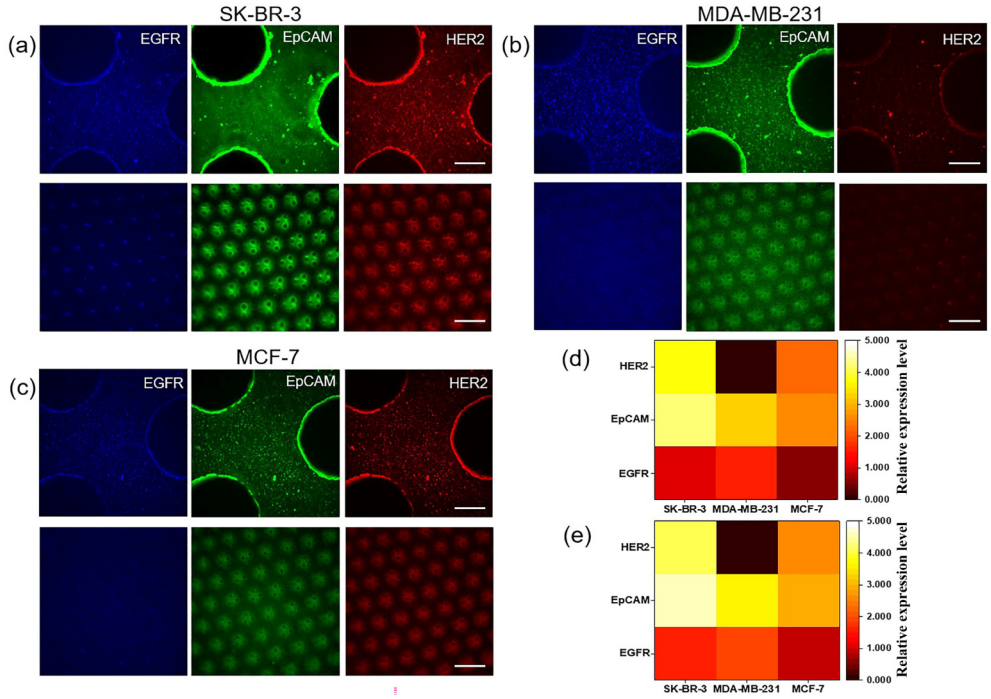

Figure 7 Breast cancer subtype analysis based on bionic compound eye imaging. (a)–(c) Imaging results of the three membrane proteins on SK-BR-3, MDA-MB-231, and MCF-7 extracellular vesicles obtained respectively using a microscopy objective lens and a bionic compound eye. (d) and (e) Expression levels of EGFR, EpCAM, and HER2 proteins on extracellular vesicles of different types (SK-BR-3, MDA-MB-231, MCF-7) obtained through direct imaging with a microscopy objective lens and bionic compound eye imaging. Scale bar: 100 μm.

fluorescence imaging of exosomal membrane proteins. Dual-color fluorescence colocalization made the imaging results more reliable. Additionally, we used 3D printing to create an arched microfluidic array chip for exosome capture and fluorescence labeling, which could be combined with the bionic compound eye for multi-angle, large FOV imaging. The results showed that the observable area of the large FOV fluorescence images obtained using the bionic compound eye was about eight times larger than that obtained with the microscopy objective alone, increasing the number of observable exosome samples. The standard deviation of the average fluorescence intensity analysis was reduced to about 38%, enabling more accurate exosome quantification with LFDF imaging. Furthermore, the feasibility of LFDF imaging for breast cancer subtype cell classification was also validated. This study demonstrated the potential application of the bionic compound eye in precise cancer diagnostics, providing a new low-cost, high-accuracy detection method in the field of exosome-based tumor diagnostics.

4 Experimental section

4.1 Materials

PBS (10 mM, pH 7.4), PEI (408727), DMEM high glucose culture medium, penicillin-streptomycin, and L-15 medium were purchased from Nanjing KeyGen Biotechnology Co., Ltd. Ethanol (100%) was purchased from Sinopharm Chemical Reagent Co., Ltd. GA (50%) was purchased from MACKLIN Company. Exosome-depleted fetal bovine serum was purchased from System Biosciences (SBI). Trichlorosilane and bovine serum albumin (BSA, 98%) were purchased from Sigma-Aldrich. Silicone elastomer and silicone elastomer curing agent were purchased from Dow Chemical Company. The reagents used in the experiment did not need further purification operations, and the deionized water used in the experiment was 18.25 MΩ·cm (Millipore Milli-Q grade) pure water. The human breast cancer cells SK-BR-3 and MDA-MB-231 were both purchased from the Cell Bank of Shanghai Institutes for Biological Sciences, Chinese Academy of Sciences. The amino-modified CD63 aptamer (5'-CAC-CCC-ACC-TCG-CTC-CCG-TGA-CAC-TAA-TGC-TA-$(CH_2)_6$-NH_2-3'), Cy5-modified HER2 aptamer (5'-Cy5-GGG-CCG-TCG-AAC-ACG-AGC-ATG-GTG-CGT-GGA-CCT-AGG-ATG-ACC-TGA-GTA-CTG-TCC-3'), Alexa Fluor 568-modified EpCAM aptamer (5'-Alexa Fluor 568-TTC-ACT-ACA-GAG-GTT-GCG-TCT-GTC-CCA-CGT-TGT-CAT-GGG-GGG-TTG-GCC-TGT-3'), and FAM-modified EGFR aptamer (5'-FAM-TGC-CGT-TTC-TTC-TCT-TTC-GCT-TTT-TTT-GCT-TTT-GAG-CAT-G-3') were synthesized by Sangon Biotech (Shanghai) Co., Ltd.

4.2 Preparation of bionic compound eye

The silicone elastomer and a silicone elastomer curing agent were mixed in a ratio of 10:1, thoroughly removing air bubbles to prepare PDMS. The PDMS was poured into a plastic dish to a thickness of 1.5 mm. The PDMS was preheated at 65 °C for 5 min, then the dissected compound eyes from fly specimens were placed onto the PDMS. The PDMS and the compound eyes were heated together at 65 °C for an additional 30 min to transfer the natural compound eye structure onto the PDMS compound eye mold.

To prevent adhesion between the mold and the PDMS during the subsequent molding step, hydrophobic treatment of the mold was necessary. The PDMS bionic compound eye mold was placed into an oxygen plasma cleaner for 90 s (parameters: oxygen flow rate of 80 sccm, alternating current of 100 W at 50 kHz). Subsequently, 15 μL of trichlorosilane was added into a vacuum chamber together with the bionic compound eye mold for silanization treatment for 3 h. The mold surface residue of

trichlorosilane with alcohol was rinsed to obtain a hydrophobically treated concave compound eye mold. Finally, PDMS was prepared and poured into the compound eye mold. The PDMS and the compound eye mold were heated together at 65 °C for 40 min. Then the cured PDMS was demolded to obtain a bionic compound eye suitable for experimentation.

4.3 Extracellular vesicle extraction

After seeding SK-BR-3 and MDA-MB-231 cells in cell culture flasks, they were placed in a CO_2 incubator and cultured until reaching a cell density of 70%. The culture medium for SK-BR-3 cells consisted of a mixture of 10% fetal bovine serum (GIBCO) and 1% penicillin-streptomycin in DMEM medium, while the culture medium for MDA-MB-231 cells was a mixture of 10% exosome-depleted fetal bovine serum and 90% L-15 medium.

The supernatant from the culture flasks was collected and centrifuged (3000*g*, 15 min, 4 °C) to remove cells and cell debris from the culture medium. After centrifugation, the supernatant was collected and centrifuged again (10,000*g*, 45 min, 4 °C) to separate extracellular vesicles (EVs) from larger vesicles as an initial purification step. Subsequently, the obtained supernatant was centrifuged at 150,000*g* for 70 min at 4 °C to extract tumor cell-derived EVs. After removing the supernatant, the collected EVs were washed with PBS (PBS used was filtered through an organic medium filter) to remove protein impurities and further purified by centrifugation (150,000*g*, 70 min, 4 °C). After removing the supernatant again, the purified EVs were resuspended in 100 μL of PBS and stored in a –72 °C freezer for future use.

4.4 Preparation of flexible PDMS microfluidic chip

The boat-shaped microfluidic chip model with a micro-pillar array was designed using SolidWorks, then the model was imported into a 3D printer to print the chip mold. Before molding, the mold needed to be treated with electronic fluorine solution for 5 min of ultrasonic treatment on the resin chip. PDMS was prepared and poured into a plastic dish containing the microfluidic chip mold. Due to the small structures of the mold, it needed to be placed in a 65 °C oven for 4 h to fully cure the PDMS micro-pillars. After curing, the PDMS was cut into chips and punch holes. They were treated with an oxygen plasma cleaner for 90 s (parameters: alternating current of 100 W at 50 kHz, oxygen flow rate of 80 sccm). The treated PDMS chip was bonded with another flat PDMS sheet to create a PDMS chip for extracellular vesicle capture and detection.

4.5 Extracellular vesicle capture and fluorescent labeling

Firstly, extracellular vesicles were captured in the microfluidic chip. 1% PEI solution (15 μL) was injected into the channel at a flow rate of 0.5 μL/min and incubated for 10 min. Then, the excess PEI was flushed out by injecting PBS solution into the channel at a flow rate of 3 μL/min. Subsequently, 5% glutaraldehyde solution (15 μL) was injected into the channel at a flow rate of 0.5 μL/min and incubated for 30 min, followed by washing with PBS solution. Then, amino-modified CD63 aptamer (15 μL, 1 μM) was injected into the channel at a flow rate of 0.5 μL/min and was incubated for 10 min, followed by washing with PBS solution. Next, 1% BSA solution (15 μL) was injected into the channel at a flow rate of 0.5 μL/min and was incubated for 30 min to block nonspecific binding sites, followed by washing with PBS solution. Then, 1 μL of extracellular vesicle stock solution was diuted in 99 μL of PBS solution, the diluted extracellular vesicle sample (15 μL) was injected into the channel at a flow rate of 0.5 μL/min, and incubated for 10 min to capture extracellular vesicles on the channel surface, followed by washing with PBS solution.

Next, the proteins on the surface of extracellular vesicles were labeled. EpCAM aptamer modified with Alexa Fluor 568 (15 μL, 1 μM) was injected into the channel at a flow rate of 0.5 μL/min and was incubated for 10 min to label the EpCAM protein on the surface of extracellular vesicles, followed by washing with PBS solution. HER2 aptamer modified with Cy5 (15 μL, 1 μM) was injected into the channel at a flow rate of 0.5 μL/min and was incubated for 10 min to label the HER2 protein on the surface of extracellular vesicles. EGFR aptamer modified with FAM (15 μL, 1 μM) was injected into the channel at a flow rate of 0.5 μL/min and was incubated for 10 min to label the EGFR protein on the surface of extracellular vesicles. Finally, the channel with PBS solution was washed, and the PDMS chip under a microscopy for fluorescence imaging was placed.

4.6 Instruments

Images were acquired using a Zeiss Elyra P.1 microscopy equipped with 405 nm (100 mW) laser, 488 nm (100 mW), 561 nm (100 mW) laser, 642 nm (100 mW) laser, 10×/0.3 DICI objective and an Andor EM-CCD camera (iXon DU897). Images of the HER2 protein were obtained using 642 nm excitation with a 655 nm longpass filter. Images of the EpCAM Protein were obtained using 561 nm excitation with a 570–640 nm bandpass filter. Images of the EGFR protein were obtained using 488 nm excitation with a 495–550 nm bandpass filter. The exposure time for each frame was 100 ms.

Electronic Supplementary Material: Supplementary material (including characterization of SK-BR-3 exosomes and reproducibility validation of LFDF method) is available in the online version of this article at https://doi.org/10.26599/NR.2025.94907203.

Data availability

All data needed to support the conclusions in the paper are presented in the manuscript and the Electronic Supplementary Material. Additional data related to this paper may be requested from the corresponding author upon request.

Acknowledgements

This work was supported by the Natural Science Foundation of China (NSFC) (Nos. 62175027, 62175030, 62205053, and 62305054).

Declaration of competing interest

All the contributing authors report no conflict of interests in this work.

Author contribution statement

Y. Y. L.: Data curation, validation, writing manuscript, experimental design. J. X. W.: Method guidance. T. Y. W.: Experimental sample provision. X. M. L.: Data analysis guidance. K. Y.: Method guidance, funding acquisition. Z. Y. W.: Funding acquisition. L. W.: Provision of equipment, manuscript revision, funding acquisition. S. F. Z.: Funding acquisition, method guidance, project

administration, manuscript revision. Y. P. C.: Funding acquisition. All the authors have approved the final manuscript.

Use of AI statement

None.

References

[1] Azmi, A. S.; Bao, B.; Sarkar, F. H. Exosomes in cancer development, metastasis, and drug resistance: A comprehensive review. *Cancer Metastasis Rev.* **2013**, *32*, 623–642.

[2] Sandfeld-Paulsen, B.; Jakobsen, K. R.; Bæk, R.; Folkersen, B. H.; Rasmussen, T. R.; Meldgaard, P.; Varming, K.; Jørgensen, M. M.; Sorensen, B. S. Exosomal proteins as diagnostic biomarkers in lung cancer. *J. Thorac. Oncol.* **2016**, *11*, 1701–1710.

[3] Joshi, G. K.; Deitz-McElyea, S.; Liyanage, T.; Lawrence, K.; Mali, S.; Sardar, R.; Korc, M. Label-free nanoplasmonic-based short noncoding RNA sensing at attomolar concentrations allows for quantitative and highly specific assay of microRNA-10b in biological fluids and circulating exosomes. *ACS Nano* **2015**, *9*, 11075–11089.

[4] Yu, Y. R.; Chen, D.; Yang, Y. B.; Yuan, Q. Recent progress in electrochemical biosensors based on DNA-functionalized nanomaterials. *Nano Biomed. Eng.* **2024**, *16*, 309–330.

[5] Doyle, L. M.; Wang, M. Z. Overview of extracellular vesicles, their origin, composition, purpose, and methods for exosome isolation and analysis. *Cells* **2019**, *8*, 727.

[6] Willms, E.; Johansson, H. J.; Mäger, I.; Lee, Y.; Blomberg, K. E. M.; Sadik, M.; Alaarg, A.; Smith, C. I. E.; Lehtiö, J.; El Andaloussi, S. et al. Cells release subpopulations of exosomes with distinct molecular and biological properties. *Sci. Rep.* **2016**, *6*, 22519.

[7] Kuang, J. J.; Fu, Z. B.; Sun, X. Z.; Lin, C. H.; Yang, S. L.; Xu, J. Y.; Zhang, M.; Zhang, H. Y.; Ning, F. H.; Hu, P. A colorimetric aptasensor based on a hemin/EpCAM aptamer DNAzyme for sensitive exosome detection. *Analyst* **2022**, *147*, 5054–5061.

[8] Park, J.; Park, J. S.; Huang, C. H.; Jo, A.; Cook, K.; Wang, R.; Lin, H. Y.; Van Deun, J.; Li, H. Y.; Min, J. et al. An integrated magneto-electrochemical device for the rapid profiling of tumour extracellular vesicles from blood plasma. *Nat. Biomed. Eng.* **2021**, *5*, 678–689.

[9] Meng, D.; Ma, W.; Wu, X. L.; Xu, C. L.; Kuang, H. DNA-driven two-layer core-satellite gold nanostructures for ultrasensitive MicroRNA detection in living cells. *Small* **2020**, *16*, 2000003.

[10] Li, B.; Liu, C. C.; Pan, W. L.; Shen, J. L.; Guo, J. Y.; Luo, T. T.; Feng, J. J.; Situ, B.; An, T. X.; Zhang, Y. et al. Facile fluorescent aptasensor using aggregation-induced emission luminogens for exosomal proteins profiling towards liquid biopsy. *Biosens. Bioelectron.* **2020**, *168*, 112520.

[11] Jiang, J. L.; Cui, X. Y.; Huang, Y. X.; Yan, D. M.; Wang, B. S.; Yang, Z. Y.; Chen, M. R.; Wang, J. H.; Zhang, Y. N.; Liu, G. et al. Advances and prospects in integrated nano-oncology. *Nano Biomed. Eng.* **2024**, *16*, 152–187.

[12] Zhang, Y.; Tong, X. D.; Yang, L.; Yin, R. L.; Li, Y.; Zeng, D.; Wang, X. Y.; Deng, K. A herringbone mixer based microfluidic device ^{HB}EXO-chip for purifying tumor-derived exosomes and establishing miRNA signature in pancreatic cancer. *Sens. Actuators B: Chem.* **2021**, *332*, 129511.

[13] Zhou, S. S.; Hu, T.; Zhang, F.; Tang, D. Z.; Li, D. K.; Cao, J.; Wei, W.; Wu, Y. F.; Liu, S. Q. Integrated microfluidic device for accurate extracellular vesicle quantification and protein markers analysis directly from human whole blood. *Anal. Chem.* **2020**, *92*, 1574–1581.

[14] Lee, G. J.; Choi, C.; Kim, D. H.; Song, Y. M. Bioinspired artificial eyes: Optic components, digital cameras, and visual prostheses. *Adv. Funct. Mater.* **2018**, *28*, 1705202.

[15] Wu, S. D.; Jiang, T.; Zhang, G. X.; Schoenemann, B.; Neri, F.; Zhu, M.; Bu, C. G.; Han, J. D.; Kuhnert, K. D. Artificial compound eye: A survey of the state-of-the-art. *Artif. Intell. Rev.* **2017**, *48*, 573–603.

[16] Li, H. F.; Gong, X. W.; Ni, Q. L.; Zhao, J. L.; Zhang, H. S.; Wang, T. S.; Yu, W. X. Replication and characterization of the compound eye of a fruit fly for imaging purpose. *Appl. Phys. Lett.* **2014**, *105*, 143705.

[17] Zhang, H.; Li, L.; McCray, D. L.; Scheiding, S.; Naples, N. J.; Gebhardt, A.; Risse, S.; Eberhardt, R.; Tünnermann, A.; Yi, A. Y. Development of a low cost high precision three-layer 3D artificial compound eye. *Opt. Express* **2013**, *21*, 22232–22245.

[18] Tanida, J.; Shogenji, R.; Kitamura, Y.; Yamada, K.; Miyamoto, M.; Miyatake, S. Color imaging with an integrated compound imaging system. *Opt. Express* **2003**, *11*, 2109–2117.

[19] Duparré, J.; Dannberg, P.; Schreiber, P.; Bräuer, A.; Tünnermann, A. Thin compound-eye camera. *Appl. Opt.* **2005**, *44*, 2949–2956.

[20] Cheng, Y.; Cao, J.; Zhang, Y. K.; Hao, Q. Review of state-of-the-art artificial compound eye imaging systems. *Bioinspir. Biomim.* **2019**, *14*, 031002.

[21] Kamal, W.; Lin, J. D.; Elston, S. J.; Ali, T.; Castrejón-Pita, A. A.; Morris, S. M. Electrically tunable printed bifocal liquid crystal microlens arrays. *Adv. Mater. Interfaces* **2020**, *7*, 2000578.

[22] Ma, Z. C.; Hu, X. Y.; Zhang, Y. L.; Liu, X. Q.; Hou, Z. S.; Niu, L. G.; Zhu, L.; Han, B.; Chen, Q. D.; Sun, H. B. Smart compound eyes enable tunable imaging. *Adv. Funct. Mater.* **2019**, *29*, 1903340.

[23] Cao, J. J.; Hou, Z. S.; Tian, Z. N.; Hua, J. G.; Zhang, Y. L.; Chen, Q. D. Bioinspired zoom compound eyes enable variable-focus imaging. *ACS Appl. Mater. Interfaces* **2020**, *12*, 10107–10117.

[24] Cogal, O.; Leblebici, Y. An insect eye inspired miniaturized multi-camera system for endoscopic imaging. *IEEE Trans. Biomed. Circuits Syst.* **2017**, *11*, 212–224.

[25] Shi, C. Y.; Wang, Y. Y.; Liu, C. Y.; Wang, T. S.; Zhang, H. X.; Liao, W. X.; Xu, Z. J.; Yu, W. X. SCECam: A spherical compound eye camera for fast location and recognition of objects at a large field of view. *Opt. Express* **2017**, *25*, 32333–32345.

[26] Cao, A. X.; Pang, H.; Zhang, M.; Shi, L. F.; Deng, Q. L.; Hu, S. Design and fabrication of an artificial compound eye for multi-spectral imaging. *Micromachines* **2019**, *10*, 208.

[27] Shen, M. J.; Di, K. L.; He, H. Z.; Xia, Y. Y.; Xie, H.; Huang, R. R.; Liu, C.; Yang, M.; Zheng, S. Y.; He, N. Y. et al. Progress in exosome associated tumor markers and their detection methods. *Mol. Biomed.* **2020**, *1*, 3.

[28] Kim, S.; Choi, B. H.; Shin, H.; Kwon, K.; Lee, S. Y.; Yoon, H. B.; Kim, H. K.; Choi, Y. Plasma exosome analysis for protein mutation identification using a combination of raman spectroscopy and deep learning. *ACS Sens.* **2023**, *8*, 2391–2400.

[29] Wu, Y.; Gao, Z. B.; Chai, Y. R.; Zhang, A. A.; He, S. T.; Liu, X.; Yuan, H. J.; Tan, L. L.; Ding, L. H.; Wu, Y. J. One-step and label-free ratiometric fluorescence assay for the detection of plasma exosome towards cancer diagnosis. *Talanta* **2024**, *271*, 125700.

[30] Cui, H. Y.; Zheng, T. F.; Qian, N. N.; Fu, X. Q.; Li, A. J.; Xing, S.; Wang, X. F. Aptamer-functionalized magnetic Ti_3C_2 based nanoplatform for simultaneous enrichment and detection of exosomes. *Small* **2024**, *20*, 2402434.

[31] Liu, M. X.; Zhang, H.; Zhang, X. W.; Chen, S.; Yu, Y. L.; Wang, J. H. Nanozyme sensor array plus solvent-mediated signal amplification strategy for ultrasensitive ratiometric fluorescence detection of exosomal proteins and cancer identification. *Anal. Chem.* **2021**, *93*, 9002–9010.

[32] Ding, L. H.; Liu, L. E.; He, L. L.; Effah, C. Y.; Yang, R. Y.; Ouyang, D. X.; Jian, N. G.; Liu, X.; Wu, Y. J.; Qu, L. B. Magnetic-nanowaxberry-based simultaneous detection of exosome and exosomal proteins for the intelligent diagnosis of cancer. *Anal. Chem.* **2021**, *93*, 15200–15208.

[33] Meng, X. D.; Lv, H. Y.; Zhang, X. J.; Zhang, M. Q. Dual signal Amplification-Mediated Aptamer-Based electrochemical biosensor for sensitive detection of exosomes. *Microchem. J.* **2024**, *207*, 112095.